

Dynamics and Depletion in Thermally Supercritical Starless Cores

Eric Keto^{1*} and Paola Caselli²

¹*Harvard-Smithsonian Center for Astrophysics, 160 Garden St, Cambridge, MA 02420, USA*

²*School of Physics and Astronomy, University of Leeds, Leeds LS2 9JT, UK*

July 7, 2009

ABSTRACT

In previous studies we identified two classes of starless cores, thermally subcritical and supercritical, distinguished by different dynamical behavior and internal structure. Here we study the evolution of the dynamically-unstable, thermally-supercritical cores by means of a numerical hydrodynamic simulation that includes radiative equilibrium and simple molecular chemistry. From an initial state as an unstable Bonnor-Ebert (BE) sphere, a contracting core evolves toward the configuration of a singular isothermal sphere (SIS) by inside-out collapse. We identify a characteristic radius, the product of the sound speed and the free-fall time, as the radius within which the density profile of a BE sphere becomes flat. We follow the gas temperature and abundance of CO during the contraction. The temperature is predominantly determined by radiative equilibrium, but in the rapidly contracting center of the core, compressive heating raises the gas temperature by a few degrees over its value in static equilibrium. The time scale for the equilibration of CO depends on the gas density and is everywhere shorter than the dynamical timescale. The result is that the dynamics do not much affect the abundance of CO which is always close to that of a static sphere of the same density profile. We use our non-LTE radiative transfer code MOLLIE to predict observable CO and N_2H^+ line spectra, including the non-LTE hyperfine ratios of N_2H^+ , during the contraction. These are compared against observations of the starless core L1544. The comparison indicates that the dust in L1544 has an opacity consistent with ice-covered rather than bare grains, the cosmic ray ionization rate is about $1 \times 10^{-17} \text{ s}^{-1}$, and the density structure of L1544 is approximately that of a Bonnor-Ebert sphere with a maximum central density of $2 \times 10^7 \text{ cm}^{-3}$, equivalent to an average density of $3 \times 10^6 \text{ cm}^{-3}$ within a radius of 500 AU. The observed CO line widths and intensities are reproduced if the CO desorption rate is about 30 times higher than the rate expected from cosmic-ray strikes alone, indicating that other desorption processes are also active.

1 INTRODUCTION

The starless cores are well described as small, dense, self-gravitating clouds supported largely but not entirely by thermal pressure. They are significant in the interstellar medium as the future birthplaces of stars. In previous papers (Keto & Field 2005; Keto & Caselli 2008) we developed a simple model to describe the temperature, density, chemistry, and dynamical evolution of the starless cores. Those studies suggest that the starless cores can be conceptually divided into two classes, thermally subcritical and thermally supercritical depending on whether their central densities are very roughly less or greater than a few 10^5 cm^{-3} respectively. This density is significant as the approximate value of two critical densities in the physics of starless cores. First, at this density gas cooling by collisional coupling with dust is about as efficient as cooling by molecular line radiation. The gas temperature in the center of the supercritical cores is therefore significantly lower than in their envelopes and

lower than found anywhere in the subcritical cores. Second, at this density, cores of a few M_\odot are at critical dynamical stability with respect to gravitational collapse. The thermally subcritical cores are stable against gravitational collapse and their dynamics may be dominated by oscillations (Lada et al. 2003; Aguti et al. 2007). In contrast, the supercritical cores are unstable with predominantly inward velocities (Williams et al. 1999; Caselli et al. 2002; Keto et al. 2004; Sohn et al. 2007; Schnee et al. 2007)

In previous papers (Keto et al. 2006; Broderick et al. 2007, 2008) we modeled the internal oscillations (sound waves) in thermally subcritical cores and computed some observable molecular spectral line profiles during the oscillations. In this paper, we model the dynamical and chemical evolution of a thermally supercritical core and compute observable molecular spectral line emission during the early stages of gravitational contraction leading up to free-fall collapse.

Our model is a one-dimensional numerical hydrodynamics code (Keto & Field 2005) that includes the radiative equilibrium of dust, gas cooling by both molecular lines and collisional coupling with the dust, and a simplified molecular chemistry (Keto & Caselli 2008). To compare the model with observations we use our numerical code for non-LTE radiative transfer MOLLIE to predict the observable molecular spectral line emission (Keto et al. 2004). That paper describes a method for modeling overlapping hyperfine emission that assumes that the hyperfine components are in statistical equilibrium. Here we use an updated algorithm that does not make this assumption and better reproduces the non-LTE hyperfine line ratios (excitation anomalies) that are seen in N_2H^+ spectra from many of the starless cores (Caselli et al. 1995; Daniel et al. 2007). We compare these predictions to previous observations of one specific core, L1544 whose properties place it in the thermally supercritical class.

There has been some considerable research into the topic of how gas clouds contract to form protostars including some classic papers in the field (Heneyey et al. 1955; Hayashi 1961; Larson 1969; Shu 1977). More recent studies also address the chemical evolution of the starless cores using a variety of models for the dynamics of gravitationally contracting cores.

Aikawa et al. (2001, 2003) followed the chemical evolution of a gravitationally collapsing core assuming the Larson-Penston (LP) approximation for the densities and velocities. In a subsequent paper, Aikawa et al. (2005) improved on this model using a numerical hydrodynamic code (Ogino et al. 1999) to follow the collapse of an isothermal Bonnor-Ebert (BE) sphere. Evans et al. (2001) showed that in the case of static BE spheres there was little difference between the structure of an isothermal BE sphere and one in radiative equilibrium. Our numerical hydrodynamic simulation that allows for radiative equilibrium during collapse suggests that the isothermal approximation used in Aikawa et al. (2005) is quite adequate for dynamic as well as static BE spheres (our §2.2). However, if we go on to predict molecular line strengths from the model cores, we need to consider temperature variations. Our §4 discusses the spectral line modeling.

Rawlings & Yates (2001) used the similarity solution of the collapse of a singular isothermal sphere (SIS) (Shu 1977) in their study of chemical evolution. Tsamis et al. (2008) combined this model for the dynamics with a model for the internal temperature structure of a BE sphere from Evans et al. (2001). Lee et al. (2004) approximated the contraction of a BE sphere as a progression of static spheres of increasing central density. Our hydrodynamic simulation suggests that this series of static equilibria is a good approximation during the subsonic phase of contraction, and that the SIS model is a good approximation at the endpoint of this phase. (our §2).

Van Weeren et al. (2009) and Brinch et al. (2008) modeled the chemical evolution during the formation of a 2D rotating accretion disk and protostar. Our spherical model applies to earlier evolutionary times while the contracting core still maintains its BE structure.

Li et al. (2002) and Shematovich et al. (2003) followed the chemical evolution during the contraction of cores that are supported by a spherical approximation of magnetic

pressure. The contraction is controlled by leakage of the magnetic field out of the core by ambipolar diffusion. In the spherical approximation, this is modeled by a diffusion equation in Lagrangian coordinates (equation 3 of Li et al. 2002). One difficulty with assessing the applicability of spherical models of magnetic collapse is that the approximation of spherical symmetry results in a density structure that, similar to the SIS and BE spheres, can be approximated by a polytrope with an index that depends on the effective equation of state. Observationally, it is difficult to distinguish polytropes of different index because their density structures are most different from one another at small and large radii where the observations have difficulties with angular resolution and sensitivity (low density gas) respectively.

In contrast, there is strong observational motivation for the model of thermal support. Masses, densities, and temperatures estimated in surveys of starless cores suggest that thermal energy provides about 75% of the internal energy required for equilibrium (Fuller & Myers 1993; Lada et al. 2008). The remaining 25% could be in magnetic energy or wave energy or a combination of both. While the 25% non-thermal energy is important for the dynamical stability and evolution of the core, the structure of the core is determined largely by the dominant thermal energy.

Our study is different from previous studies in that we consider the evolution of a BE sphere rather than an accretion disk plus protostar, or an SIS sphere, or a magnetically supported sphere, and we follow the dynamics of the contraction simultaneously and self-consistently with radiative equilibrium and a simple model for the chemistry that allows for changes in the molecular line cooling as the molecular abundances in the gas phase change with time. In this paper, we first discuss the dynamics of the gravitational contraction of a BE sphere. Our code is best suited for subsonic velocities and we confine our discussion to the early phase of evolution. We then discuss how the gas phase abundance of CO evolves during contraction. We predict how the molecular line strengths should vary across the model from center to edge, at different times during the contraction, and we compare this prediction with ratios of line strengths previously observed in L1544. We intend the comparison in a general sense only and not in detail. For example, the model is spherically symmetric while both the observed morphology (Ward-Thompson, Motte, & André 1999; Bacmann et al. 2000) and observed spectra (Williams et al. 1999; Caselli et al. 2002; Williams et al. 2006) indicate that both the density and velocity structure of L1544 are more complex than can be reproduced by a purely spherical model.

2 THE GRAVITATIONAL CONTRACTION OF AN UNSTABLE BONNOR-EBERT SPHERE

We model a core of $10 M_\odot$ that begins its evolution with an initial density of $2 \times 10^4 \text{ cm}^{-3}$ in a state of radiative and dynamical equilibrium. The mass and density place the core in the thermally supercritical class (figure 14 of Keto & Caselli 2008) so that the dynamical equilibrium is unstable. Based on the results of Keto & Caselli (2008) we use our higher

dust opacities that are equal to four times the standard dust opacities of Ossenkopf & Henning (1994), and we use a rate of cosmic ray ionization of $1.3 \times 10^{-17} \text{ s}^{-1}$ referred to as the "low" rate in Keto & Caselli (2008). In that investigation, this combination was found to result in gas temperatures that match those suggested by the observations of Crapsi et al. (2007) at their suggested central density of $2 \times 10^6 \text{ cm}^{-3}$.

Figures 1 and 2 show the density and velocity profiles during contraction as the central density increases from its initial value to $2 \times 10^8 \text{ cm}^{-3}$ over a time period of 1 Myr. The shapes of the density and velocity profiles that are generated by the numerical simulation can be understood in terms of relatively simple theory. We begin with the density profile.

2.1 The density profile

The density profiles in figure 1 show an outer region where the density scales as r^{-2} and an inner region where the density is nearly constant. As the evolving core contracts, the density profile maintains this shape even as the central density increases (Larson 1969; Hunter 1977; Foster & Chevalier 1993; Ogino et al. 1999; Kandori et al. 2005). Thus we should expect to observe this characteristic shape in almost all starless cores, and this is generally confirmed by observations. Ward-Thompson et al. (1994), Andr e et al. (1996), Ward-Thompson, Motte, & Andr e (1999), and Bacmann et al. (2000) suggested that the density profiles derived from observations of dust emission could be well matched by two power laws, one shallow and one steep. This approximation is also suggested by the numerical studies of the contraction of a BE sphere cited above. Tafalla et al. (2002, §4.2) suggested that the density profile can be better fit by,

$$\rho(r) = \frac{\rho_c}{1 + (r/r_f)^\alpha} \quad (1)$$

where r_f is the radius of the inner region.

2.1.1 The flat inner region

In the center of a BE sphere, where the sound-crossing time is less than the free-fall time, density perturbations are rapidly smoothed by pressure waves. Also the self-gravity in the center is relatively weak so that the gas is essentially confined by the pressure of the overlying gas. Both these effects act to maintain constant density around the center.

Previously, the size of the region with a flat density profile, r_f , was determined empirically for individual cores from their observations. We can also determine this radius theoretically. At r_f the ratio of the sound-crossing and free-fall times ought to be one. We find that the characteristic radius is well approximated by the product of the sound speed, a , and the free-fall time at the central density, ρ_c ,

$$r_f = \frac{a}{(32\rho_c G/3\pi)^{1/2}}. \quad (2)$$

This provides a better approximation in equation 1 than the standard scale length of a BE sphere, $[kT/(4\pi G\rho_c)]^{1/2}$ (Bonnor 1956) and is also useful in suggesting the physics behind the behavior of a contracting BE sphere.

Figure 1 compares the density profile computed by

equations 1 and 2, assuming a gas temperature of 10 K and a central density of $2 \times 10^7 \text{ cm}^{-3}$ (green curve), against the density profile computed by the numerical hydrodynamic simulation. The comparison suggests that equations 1 and 2 provide a good, simple approximation to the density profile of a BE sphere. A more accurate approximation is described in Natarajan & Lynden-Bell (1997). Because the numerical hydrodynamic simulation also accounts for a variable temperature set by radiative equilibrium, the comparison also shows that the departures from isothermal owing to radiative equilibrium have little effect on the overall density structure of the core.

Figure 1 also shows the characteristic radius, r_f , for the different evolutionary times during the contraction. The figure shows that equation 2 provides a good approximation to the turn-over radius, r_f , at all times in the evolution. According to equation 2, this width shrinks as the central density of a contracting BE sphere increases. In the subsonic phase of gravitational contraction, r_f moves at about half the maximum gas velocity where this maximum is taken from the velocity profiles for each evolutionary time as shown in figure 2.

In comparing our theoretical results to several observations, we find that a central density of about $2 \times 10^7 \text{ cm}^{-3}$ provides a better match to the observations (§4) than central densities that are a factor of 10 higher or lower. This estimate is in agreement with the density of $2 \times 10^6 \text{ cm}^{-3}$ suggested by the observations of Crapsi et al. (2007) if we average the theoretical density profile over the size of their observing beam. Although the theoretical density profile appears flat in the center of a log-log plot of density versus radius, it is sharply peaked within the size of the observing beam. The average density within a radius of 500 AU (observing beam size of 1000 AU = 7" at 140 pc) is 2.8×10^6 corresponding to a peak density of $2 \times 10^7 \text{ cm}^{-3}$. In fact, at a spatial resolution of 1000 AU, observations have difficulty measuring the central density. For example, the average density over 1000 AU corresponding to a peak density of $2 \times 10^8 \text{ cm}^{-3}$ is only $3.4 \times 10^6 \text{ cm}^{-3}$, little different from the average density of $2.8 \times 10^6 \text{ cm}^{-3}$ corresponding to a peak density of $2 \times 10^7 \text{ cm}^{-3}$.

In our previous paper (Keto & Caselli 2008), we used the lower central density of $2 \times 10^6 \text{ cm}^{-3}$ and stated that a higher central density would imply a higher density throughout the core. This is not correct. Owing to the inside-out character of the collapse, the central density increases much more rapidly than the densities outside of r_f . As explained in the next section, in an evolving core, the densities over most of the core are actually about the same for both these higher and lower central densities (figure 1).

2.1.2 The self-similar outer region

In their numerical hydrodynamic simulations of gravitationally collapsing gas clouds, Bodenheimer & Sweigart (1968) found that regardless of the initial configuration of the cloud or the initial conditions, all their examples evolved to density profiles scaling as r^{-2} in their outer regions. Shu (1977) suggests that this scaling is a property shared by all self-gravitating isothermal systems under certain general conditions. The system should evolve subsonically, meaning that it should be close to hydrostatic equilibrium initially, and

the outer region should not be affected by an outer bounding surface. These conditions are applicable to contracting BE spheres. The initial state is one of hydrostatic balance, albeit unstable. Although BE spheres have an outer boundary which is the radius at which the Lane-Emden equation is truncated, the external pressure at the boundary is the same as would be provided by the Lane-Emden equation if the solution were continued. Thus in the initial configuration, the density profile is the same as if the core had no outer boundary.

Figure 2 shows that the BE sphere evolves by subsonic contraction to resemble the SIS, a result also found in earlier studies (Larson 1969; Foster & Chevalier 1993). As the central density increases with the contraction, the characteristic radius, r_f , moves inward, the constant density region shrinks in size, and the outer region with its density profile scaling as $\rho \sim r^{-2}$ accounts for more and more of the core. Because the density of the outer region changes very slowly, the density contrast between the inner and outer regions also increases rapidly. Thus, as the contraction proceeds, the BE sphere evolves to resemble an SIS with its r^{-2} density profile everywhere and its infinite density contrast.

This behavior is expected if we recall that the static equilibrium solutions of the Lane-Emden equation form a continuous series with increasing density concentration and the SIS as the limiting case (Chandrasekhar 1957; Shu 1977). During the subsonic, quasi-static phase of contraction, an unstable BE sphere evolves approximately along this series of static equilibria toward the limiting case of an SIS.

2.2 The velocity profile and the inside-out collapse of a BE sphere

The velocity profile during the subsonic phase of the contraction of a BE sphere shows a characteristic Λ -shape with the inward velocity as a function of radius increasing from near zero in the core center to a maximum just outside the characteristic radius, r_f , before decreasing again toward the edge of the core (Foster & Chevalier 1993; Ogino et al. 1999; Kandori et al. 2005). The origin of this profile can be understood by considering the forces inside and outside of r_f . In the very center, the velocity is zero by symmetry. In the region, r_f , where the density is constant, the instantaneous acceleration due to the gravitational force increases linearly with radius. The velocity, which is the time-integrated acceleration, may also be expected to increase with radius as well, and this is verified by the numerical evolution. Outside of r_f , the density falls off as r^{-2} . Here the instantaneous gravitational acceleration decreases with radius along with its influence on the velocity. During the contraction, the redistribution of mass in the center does not change the gravitational acceleration in the outer region because of spherical symmetry. Thus, in the outer region, the only change to the hydrostatic balance is due to the pressure force which propagates outward from the center only at the sound speed. These several effects that would change the hydrostatic balance in the outer region all decrease as we move outward, away from r_f . Thus the outer region remains in approximate hydrostatic balance with low inward velocities for about a sound-crossing time, on the order of 1 Myr, and the velocities are lower at larger radii, further from r_f .

The same characteristic Λ -shaped profile also develops if

we consider the pressure-free collapse of a BE sphere. In this case the gas pressure is ignored and the velocity field is determined solely by the variation of the gravitational force with radius. (Whitworth & Ward-Thompson 2001; Myers 2005). Of course, the gas pressure is required to obtain the initial BE density distribution in the first place.

3 THE TEMPERATURE AND CHEMISTRY OF THE EVOLVING CORE

In the previous section we saw that the dynamics of a contracting BE sphere, as followed by a numerical simulation that included radiative and chemical equilibrium, were well matched by a simpler isothermal approximation. In this section we will see that the temperature and chemistry of an evolving core have a significant effect on the observable molecular line spectra. The gas temperature directly affects the line brightness through the source function. The chemistry affects the line brightness through the gas phase abundance of the observable molecules. The most significant processes affecting the abundances are the depletion of molecules from the gas phase as they freeze onto dust grains in the dense center of a core and photodissociation of molecules near the core boundary. We calculate the CO abundance with a simple model that includes these two processes (Keto & Caselli 2008).

Figure 3 shows the gas temperatures, density, velocity, and CO abundance at 3 different times during the collapse when the central density is 2×10^6 , 2×10^7 , and $2 \times 10^8 \text{ cm}^{-3}$. As discussed further in §4, a model with a central density of $2 \times 10^7 \text{ cm}^{-3}$ provides a better match to the observations than central densities that are a factor of 10 lower or higher. Also shown are the density, temperature, and abundance of static cores that have the same central densities as the dynamically evolving core. The properties of the contracting cores are similar to those of the static cores with the same central density, with the exception of the velocity.

3.1 The temperature in the center of a contracting core

The starless cores are heated from the outside by both cosmic rays and by the diffuse interstellar radiation field supplied by the population of stars in the Galaxy. The cores are cooled by the long wavelength radiation from cold dust and by molecular lines. Because the incoming shorter wavelength starlight is strongly absorbed by the cores whereas the outgoing long wavelength radiation from cold dust is not, the denser cores are coldest in their centers. This temperature structure has been calculated in quite a number of papers (references in Keto & Field 2005). In figure 3 we see that the central temperature of the static core with a central density of $2 \times 10^8 \text{ cm}^{-3}$ is quite low, below 5 K. In the evolving core, compressive heating keeps the temperature above 5 K, more consistent with the observations.

3.2 The time scale for the depletion of CO

Figure 3 shows that the abundance of CO during the contraction of a BE sphere is quite close to its steady state value. This is because the time scale for depletion of CO is

much faster than the dynamical time scale. The analysis in section 2 suggests that the dynamical time varies across the core. In the core center, the free-fall time is a close approximation whereas in the more slowly evolving outer region, the sound crossing time is more appropriate. A starless core with a mass of $10 M_{\odot}$ and a central density of $2 \times 10^6 \text{ cm}^{-3}$ has a free-fall time, $\tau_{ff} = 0.03 \text{ Myr}$ using the central density in the standard equation whereas the sound crossing time is about 2 Myr.

The time scale for CO to freeze onto dust, τ_{on} , from Rawlings et al. (1992) and the time scale for the inverse process of desorption, τ_{off} , from Hasegawa & Herbst (1993) are given as equations 8 and 11 respectively in Keto & Caselli (2008). These may be combined to determine the time scale for the change of CO in the gas phase (Caselli et al. 2002),

$$\tau_{CO} = \frac{\tau_{on}\tau_{off}}{\tau_{on} + \tau_{off}}. \quad (3)$$

The depletion time scale is density dependent. At the center of the core, $\tau_{CO} = 0.01 \text{ Myr}$ a factor of 3 shorter than the free-fall time. At the edge of the core where the density is 20 cm^{-3} , $\tau_{CO} = 0.5 \text{ Myr}$, still a factor of 4 shorter than the sound crossing time. As a result, the CO abundance approximates its steady state abundance (equation 12 Keto & Caselli 2008) throughout the contraction.

Even though the time scale for desorption is generally much slower than the time scale for depletion, general considerations require both the forward and reverse reactions. Real physical systems must satisfy detailed balance and time reversibility (Onsager 1931). A system described by a single rate equation, for example depletion only without desorption, does not satisfy these conditions, cannot describe a physical system, and this description will produce misleading results.

In the case of our simple chemical model it is straightforward to show that even though the desorption rate is very slow compared to the rate of freeze-out, different desorption rates produce different abundances. In figure 4 we show the abundance of CO obtained with 4 different desorption rates. The lowest rate is equivalent to desorption caused by the "low" cosmic ray rate ($1.3 \times 10^{-17} \text{ s}^{-1}$) as defined in Keto & Caselli (2008). The higher desorption rates are factors of 3, 9, and 30 higher than the lowest rate. The 4 curves show that the abundance depends on the desorption rate even though each of the rates is small compared to the forward rate.

In our model, we use equation 11 of Keto & Caselli (2008) in which the desorption is entirely due to the direct heating of grains by cosmic rays. However, as suggested by Roberts et al. (2007) there are two other processes that cause desorption: the exothermic formation of H_2 on the grain surface, and cosmic ray induced photodesorption. Roberts et al. (2007) suggest that the rates of these processes are not known, but they can be larger than the desorption rate due to grain heating by cosmic ray. In fact, Shen et al. (2004) found that the energy input by the cosmic ray induced ultraviolet field is almost one order of magnitude larger than the direct energy input by cosmic ray particles. Because both these processes depend on the first power of the density, the same as direct cosmic ray heating, we can account for the additional desorption processes in our model by simply increasing the desorption rate above

that given by equation 11 of Keto & Caselli (2008) while still assuming the same first-power dependence on the gas density. We find that these other processes are necessary if we are to match all the observations.

With the low value of the desorption rate, the gas phase abundance is everywhere so low that we cannot get the CO lines bright enough to match the observations. Increasing the desorption rate solves this problem. As shown in figure 4, with the highest desorption rate, the maximum CO abundance is about a factor of 2.5 higher because the higher desorption rate keeps more of the CO in the gas phase at mid-radii where photodissociation starts to become less effective. (The results for the CO abundance displayed in figure 3 refer to the case with the highest desorption rate.) This increase in abundance makes the optically thin C^{17}O and C^{18}O lines almost a factor of 2 brighter and a better match to the observations. The CO spectra are discussed in §4.

The required increased abundance and brighter lines could in principle result from a higher undepleted abundance of CO. However, the undepleted abundance would have to be about 10^{-3} to produce the same effect. This is ten times larger than the value derived by Frerking et al. (1982) in the Taurus molecular cloud complex where L1544 is embedded. Thus an increase in the desorption rate is suggested rather than an increase in the undepleted abundance. The desorption rate cannot be increased by increasing the flux of cosmic rays, but must be caused by other desorption processes. In our earlier study we found that a higher flux of cosmic rays would cause the gas temperature at mid-radii to be higher than suggested by observations (figure 12 Keto & Caselli 2008).

The gas phase abundance can also be increased by decreasing the reverse reaction of freeze-out. One way this could occur is if the dust grains in the center of L1544 were fewer in number but larger in size, for example by coagulation. This would decrease the total surface area available for freeze-out (van Dishoeck et al. 1993). There is some independent evidence for coagulated grains Caselli et al. (2002); Keto et al. (2004); Bergin et al. (2006); Flower et al. (2006); Van Weeren et al. (2009). However, to reduce the rate of freeze-out by a factor of 30, would require a mean grain diameter of about $10 \mu\text{m}$, too large according to available models of dust coagulation in dense clouds Ossenkopf & Henning (1994). Although we cannot exclude a combination of decreased depletion and increased desorption, other desorption processes besides direct cosmic-ray strikes are probably responsible for keeping the CO gas phase abundance high enough to match the observed CO line strengths.

4 COMPARISON WITH OBSERVATIONS

All other things being equal, a collisionally excited, optically thin line should increase in brightness with the path length and the gas density. Thus molecular lines should be brightest through the center of the core. Observations of starless cores do not always show this behavior because of varying molecular abundances within the core (Tafalla et al. 2002). For example, figure 2 of Caselli et al. (1999) reproduced here as figure 5 shows the brightness of the (1-0) transitions of C^{17}O , C^{18}O , and N_2H^+ at a set of positions across the L1544

core from edge to center to edge. The N_2H^+ molecule does not suffer much, if any, depletion from the gas phase at high densities, and the observed N_2H^+ brightness increases toward the core center whereas the observed CO brightness does not. This difference is due to the near complete depletion of CO at higher density. The decrease in temperature in the core center is not sufficient to significantly decrease the line brightness. It is possible that N_2H^+ may be slightly depleted in the center of L1544 (Caselli et al. 2002) although we do not include this effect in our model. We will investigate this possibility in a future modeling of higher density tracers and transitions.

Figure 6 shows the simulated integrated spectral line brightness as a trace of positions across the model evolving cores in the same format as the observational data in figure 5. The integrated intensities include the emission from all three hyperfine lines of $\text{C}^{17}\text{O}(1-0)$ and all seven hyperfine lines of $\text{N}_2\text{H}^+(1-0)$. At central densities greater than 10^6 cm^{-3} the modeled brightness begins to look like the observations. There are some differences.

The observational data might show a slight dip in the integrated intensity of the CO lines toward the center which is not present in the model. However, there is a decrease in the peak intensity of the modeled CO lines (figure 7). This dip does not show up in the integrated intensity because the line widths in the model increase toward the center owing to the increase in the inward velocities in the inside-out collapse (figures 8). The increase in the line width of N_2H^+ is greater than that of CO because, owing to depletion, there is essentially no gas phase CO in the center of the core where the velocities are highest. From a density of 2×10^6 to $2 \times 10^8 \text{ cm}^{-3}$ the C^{17}O and C^{18}O line widths increase by 0.07 and 0.06 km s^{-1} while the N_2H^+ line width increases by 0.15 km s^{-1} .

Because the density, temperature, and abundance structures of contracting cores are so similar to those of static cores, the primary observable evidence of contraction is not the line brightnesses, but rather the shapes of those spectral lines such as $\text{N}_2\text{H}^+(1-0)$ that are optically thick enough to show self-absorption. Figure 9 shows the spectral line profiles of the (1-0) transitions of C^{17}O , C^{18}O , and N_2H^+ expected from our model for the 3 evolutionary times corresponding to figure 3. As the inward velocities increase during the contraction, the N_2H^+ spectral lines become wider (figure 8), and eventually split into two peaks (figure 9) because of the inward velocities in the core (figure 3). In contrast, because there is little CO in the center where the velocities are highest, the width of the CO lines changes very little (figure 8) as the core evolves, and the CO lines do not split (figure 9). The line brightness of both the N_2H^+ and CO lines are nearly constant as the central density increases from 2×10^6 to $2 \times 10^8 \text{ cm}^{-3}$ because there is very little change in the density of most of the core except for the center where CO is depleted. The slight decrease in the peak brightness of C^{18}O (figure 7 and 9) is consistent with a constant integrated intensity and the slight increase in line width (figure 8). There is very little change in any of the observed spectra, either CO or N_2H^+ , as the core evolves from a central density of 2×10^7 to $2 \times 10^8 \text{ cm}^{-3}$ because the change is happening in a very small region in the center that does not contain much mass relative to the entire core and is also becoming small compared to the observing beam. Thus the N_2H^+

spectra (figure 9) for the last two evolutionary times look almost the same. Interferometric observations of higher density transitions of N_2H^+ and N_2D^+ will be needed to unveil the dynamical stage, structure and kinematics of the rapidly contracting center of the core. This will be investigated in a future paper.

5 CONCLUSIONS

We follow the contraction of a thermally supercritical core through the evolutionary phase of subsonic contraction with a numerical code that includes radiative and chemical equilibrium.

We identify a characteristic radius, the product of the sound speed and the free-fall time, as the point where the density profile of a BE sphere transitions from an outer region where the density scales as r^{-2} to an inner region of constant or flat density. In the inner region, the dynamical time is the gravitational free-fall time at the central density. In the outer region, the dynamical time is the much slower sound-crossing time. The difference results in inside-out collapse.

Once this characteristic radius becomes smaller than the angular resolution, observations have difficulty in determining the exact central density even if the observed molecule is not significantly depleted.

We follow the gas temperature and abundance of CO during contraction. In the rapidly contracting center of the core, compressive heating raises the gas temperature by a few degrees over its value in static equilibrium and the results are consistent with observations. The temperature variations from the radiative equilibrium do not significantly affect the dynamics of the large scale structure of the thermally supercritical core. The time scale for the equilibration of CO is everywhere shorter than the dynamical timescale. Thus, the CO abundance is always close to that of a static sphere of the same density profile.

The comparison with line profiles observed toward L1544 suggests that the dust has an opacity consistent with ice covered grains, the cosmic ray ionization rate is close to $1 \times 10^{-17} \text{ s}^{-1}$, and the maximum density is about $2 \times 10^7 \text{ cm}^{-3}$, equivalent to an average density of $3 \times 10^6 \text{ cm}^{-3}$ within a radius of 500 AU corresponding to an observing beam size of 1000 AU. The line width and intensity of C^{18}O and C^{17}O lines can be simultaneously reproduced by our model only if the CO desorption rate is about 30 times larger than the rate expected from cosmic-ray impulsive heating alone.

REFERENCES

- Aikawa, Y., Ohashi, N., Inutsuka, S.-I., Herbst, E., Takakuwa, S., 2001, *ApJ*, 552, 639
- Aikawa, Y., Ohashi, N., & Herbst, 2003, *ApJ*, 593, 906
- Aikawa, Y., Herbst, E., Roberts, H. & Caselli, P., 2005, *ApJ*, 620, 330
- Aguti, E.D., Lada, C.J., Bergin, E.A., Alves, J.F., Birkinshaw, M., 2007, *ApJ*, 665, 457
- Andr e, P., Ward-Thompson, D., Motte, F., 1996, *AA*, 314, 625
- Bacmann, A., Andr e, A.P., Puget, J.-L., Abergel, A., Bon-temps, S., & Ward-Thompson, D. 2000, *A&A*, 361, 555
- Bergin, E. A., Maret, S., van der Tak, F. F. S., Alves, J., Carmody, S. M., & Lada, C. J. 2006, *ApJ*, 645, 369
- Bodenheimer, P. & Sweigart, A., 1968, *ApJ*, 152, 515
- Bonnor, W., 1956, *MNRAS*, 116, 351
- Brinch, C., Van Weeren, R.J., & Hogerheijde, M.R., 2009, *AA*, 489, 617
- Broderick, A. E., Keto, E., Lada, C. J., & Narayan, R., 2007, *ApJ*, 671,1832
- Broderick, A. E., Narayan, R, Keto, E., & Lada, C. J., 2008, arXiv.0804.1790
- Caselli, P., Myers, P., Thaddeus, P., 1995, *ApJL*, 455, L77
- Caselli, P., Walmsley, C., Tafalla, M., Dore, L., & Myers, P. 1999, *Ap JI*, 523, 165
- Caselli, P., Walmsley, C., Zucconi, A., Tafalla, M., Dore, L., & Myers, P. 2002, *Ap J*, 565, 344
- Chandrasekhar, S., 1957, *Stellar Structure* (New York: Dover Publications)
- Crapsi, A., Caselli, P., Walmsley, M. C., & Tafalla, M. 2007, *AA*, 470, 221
- Daniel, F., Cernicharo, J., Roeff, E., Gerin, M., Dubernet, M.L., 2007, *ApJ*, 667, 980
- Evans, N., Rawlings J., Shirley, Y., & Mundy, L. 2001, *Ap J*, 557, 193
- Foster, P. & Chevalier, R., 1993, *ApJ*, 416, 303
- Flower, D. R., Pineau Des For ets, G., & Walmsley, C. M. 2006, *AA*, 456, 215
- Frerking, M. A., Langer, W. D., & Wilson, R. W. 1982, *ApJ*, 262, 590
- Fuller, G.A. & Myers, P.C., 1993, *ApJ*, 418, 273
- Hasegawa, T., & Herbst, E., 1993, *MNRAS*, 261, 83
- Hennebelle, P., 2003, *AA*, 411, 9
- Hayashi, C., 1961, *PASJ*, 13, 450
- Heney, L.G., Lelevier, R., & Levee, R.D., *PASP*, 67,154
- Hunter, C., 1977, *ApJ*, 218, 834
- Kandori, R., Nakajima, Y., Tatematsu, K., Aikawa, Y., Naoi, T., Sugitani, K., Nakaya, H., Nagayama, T., Nagata, T., Kurita, M., Nagashima, C., Sato, S., 2005, *AJ*, 130, 2166
- Keto, E., Rybicki, G., Bergin, E., Plume, R., 2004, *Ap J*, 613, 355
- Keto, E. & Caselli, P., 2008, arXiv0804.0822
- Keto, E. & Field, G., 2005, *ApJ*, 635, 1151
- Keto, E., Broderick, A., Lada, C.J., & Narayan, R., 2006, *ApJ*, 652,1366
- Lada, C. J., Bergin, E. A., Alves, J. F., & Huard, T. L. 2003, *ApJ*, 586, 286
- Lada, C.J., Muench, A.A., Rathborne, J., Alves, J.F., & Lombardi, M., 2008, *ApJ*, 672, 410
- Larson, R.,B., 1969, *MNRAS*, 145, 271
- Lee, J.-E., Bergin, E.A., Evans, N.J., 2004, *ApJ*, 617, 360
- Li, Z.-Y., Shematovich, V.I., Wiebe, D.S., & Shustov, B.M., 2002, *ApJ*, 569, 792
- Myers, P.C., 2005, *ApJ*, 623, 280
- Natarajan, P. & Lynden-Bell, D., 1997, *MNRAS*, 286,268
- Ogino, S., Tomisaka, K. & Nakamura, F., 1999, *PASJ*, 51, 637
- Onsager, L., 1931, *Phys Rev*, 37, 405
- Ossenkopf, V., & Henning, T. 1994, *AA*, 291, 943
- Penston, M.V., 1969, *MNRAS*, 144, 425
- Rawlings, J.M.C., Hartquist, T.W., Menten, C.M., Williams, D.A., 1992, *MNRAS*, 255, 471
- Rawlings, J.M.C. & Yates, J.A., 2001, *MNRAS*, 326, 1423
- Redman, M.P., Keto, E., Rawlings, J.M.C., 2006, *MNRAS*, 370, 1
- Roberts, J. F., Rawlings, J. M. C., Viti, S., & Williams, D. A. 2007, *MNRAS*, 976
- Schnee, S., Caselli, P., Goodman, A., Arce, H. G., Ballesteros-Paredes, J., & Kuchibhotla, K. 2007, *ApJ*, 671, 1839
- Shematovich, V.I., Wiebe, Shustov, B.M., & Li, Z.-Y., 2003, *ApJ*, 588, 894
- Shen, C. J., Greenberg, J. M., Schutte, W. A., & van Dishoeck, E. F. 2004, *AA*, 415, 203
- Shu, F.H., 1977, *ApJ*, 214, 488
- Sohn, J. Lee, C.W., Park, Y-S., Lee, H.M., Myers, P.C., Lee, Y., 2007, *ApJ*, 664 928
- Spitzer, L., 1978, *Physical Processes in the Interstellar Medium*, New York Wiley-Interscience
- Tafalla, M., Myers, P., Caselli, P., Walmsley, C., & Comito, C. 2002, *Ap J*, 569, 815
- Tsamis, Y.G., Rawlings, J.M.C., Yates, J.A., & Viti, S., 2008, arXiv:0803.0519
- van Dishoek, E. F., Blake, G. A., Draine, B. T., & Lunine, J. I. 1993, *Protostars and Planets III*, 163
- Van Weeren, R.J., Brinch, C., & Hogerheijde, M.R., 2009, *AA*, 497, 773
- Ward-Thompson, D., Scott, P., Hills, R., & Andr e, P. 1994, *MNRAS*, 268, 274
- Ward-Thompson, D., Motte, F., & Andr e, P. 1999, *MNRAS*, 305, 143
- Whitworth, A.P. & Ward-Thompson, D., 2001, *ApJ*, 547, 317
- Williams, J.P., Myers, P.C., Wilner, D.J., DiFrancesco, J., 1999, *ApJ*, 513, L61
- Williams, J.P., Lee, C.W., Myers, P.C., 2006, *ApJ*, 636, 952

This paper has been typeset from a \TeX / \LaTeX file prepared by the author.

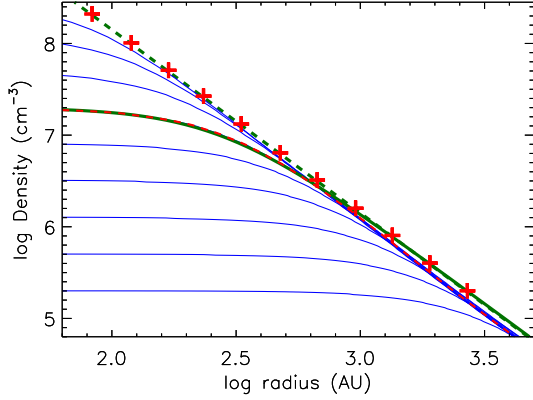


Figure 1. The progression of the density profile of a thermally supercritical starless core during subsonic contraction. The profile with a central density of $2 \times 10^7 \text{ cm}^{-3}$ (the central density of L1544) is indicated by the dashed red line. The solid green line shows how well the approximation of equation 1 fits this density profile even though the approximation assumes isothermal gas and the numerical calculation allows for temperature variations due to radiative equilibrium (figure 3). Density profiles at earlier and later times are shown in blue below and above this line. The evolution covers 1 Myr. For each profile, a cross marks the characteristic radius, r_f (equation 2) that separates the inner region with approximately constant density, and the outer region with density scaling as r^{-2} . A slope of -2 is shown as the dashed green line. Over time, as the central density increases, the characteristic radius moves inward and the BE sphere resembles more and more a singular isothermal sphere with $\rho \sim r^{-2}$ everywhere.

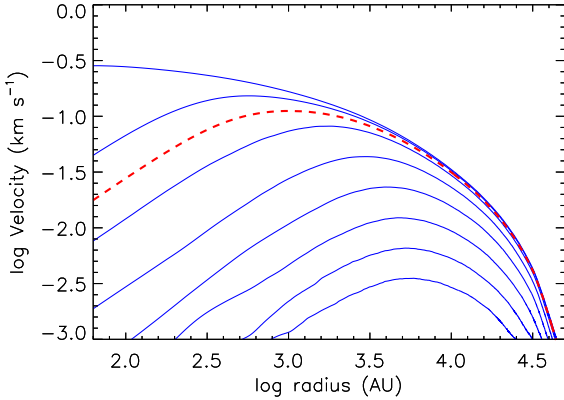


Figure 2. The progression of the velocity profile of a thermally supercritical core during subsonic contraction. The profiles have a characteristic Λ -shape with the maximum inward velocity near the characteristic radius, r_f (equation 2). The profile at the time that the central density is $2 \times 10^7 \text{ cm}^{-3}$ (the central density of L1544) is indicated by the dashed red line.

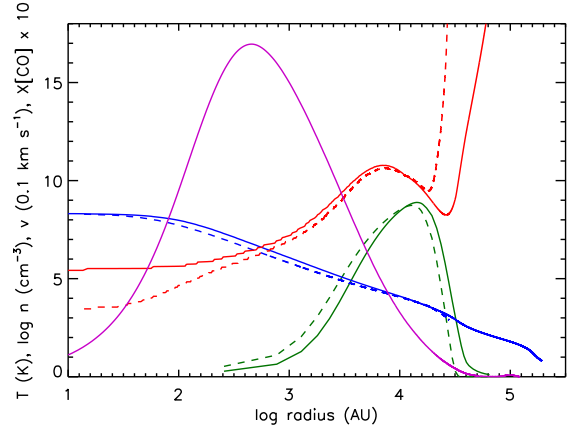
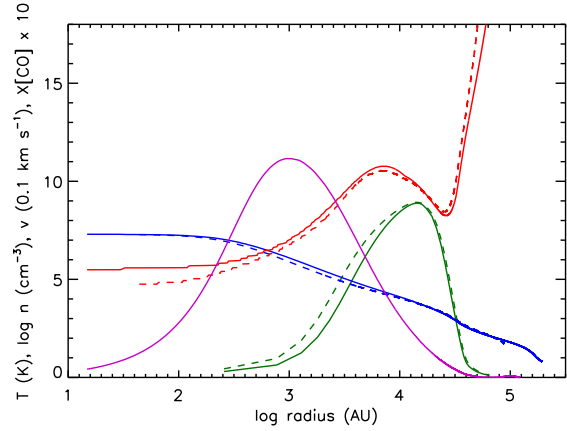
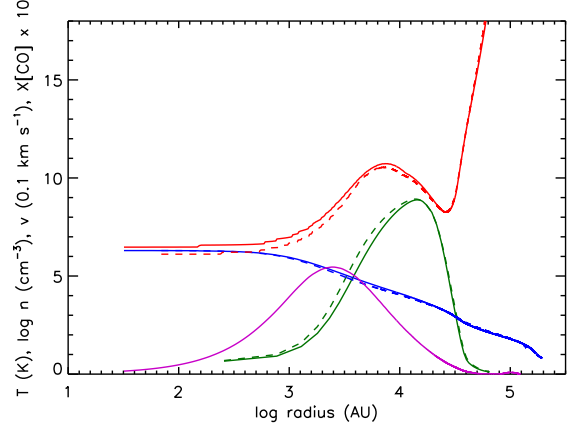


Figure 3. The temperature, density, abundance, and inward velocity profiles of a contracting starless core at 3 times in the evolution of the contraction, when the central density is $2 \times 10^6 \text{ cm}^{-3}$ (top), $2 \times 10^7 \text{ cm}^{-3}$ (middle), and $2 \times 10^8 \text{ cm}^{-3}$ (bottom). Red indicates the temperature in K, blue the log of the density in cm^{-3} , green the ratio of the CO abundance to the undepleted abundance multiplied by 10. A ratio of 10 corresponds to no depletion and zero to total depletion. Purple indicates the inward velocity. In this figure a positive velocity is inward, and the velocity units are 0.1 km s^{-1} . The dashed lines show the temperature, density, and abundance of a static sphere with the same central density. The subsonically contracting sphere closely resembles the static sphere except for the velocities.

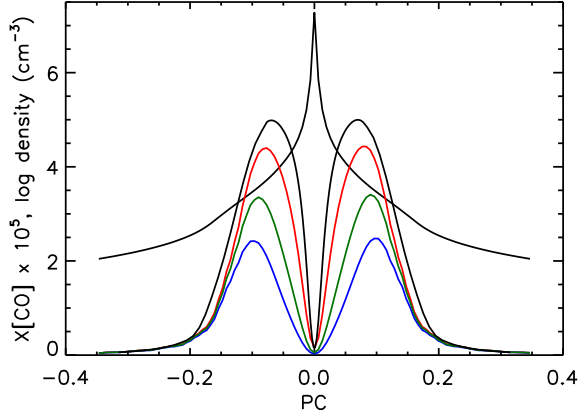


Figure 4. The abundance of CO for different rates of desorption. The black line peaking at the center of the core shows the log of the density (cm^{-3}). The other 4 curves show the abundance calculated from an equilibrium between freeze-out, desorption, and photodissociation for 4 different rates of desorption (§3.2). The lowest rate of desorption (blue curve) results in a CO abundance that is too low to match the observed CO line brightness. The highest rate of desorption (black curve) results in spectral line models that best match the observations.

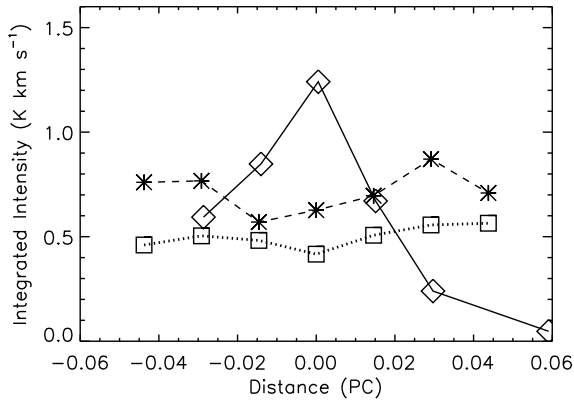


Figure 5. Observations of the trace of the integrated intensity of $\text{C}^{18}\text{O}(1-0)$ (boxes and dotted line), $\text{C}^{17}\text{O}(1-0)$ (stars and dashed line), and $\text{N}_2\text{H}^+(1-0)$ (diamonds and solid line) across L1544 from Caselli et al. (1999). The N_2H^+ molecule is not much depleted, if at all, at high densities, and its emission peaks toward the center of L1544. In contrast the lines of CO, a molecule that is subject to depletion, are approximately constant across the core, possibly with lower intensity toward the center. The N_2H^+ emission has been divided by 5.65 and the C^{18}O emission by 3.65, to match figure 2 in Caselli et al. (1999)

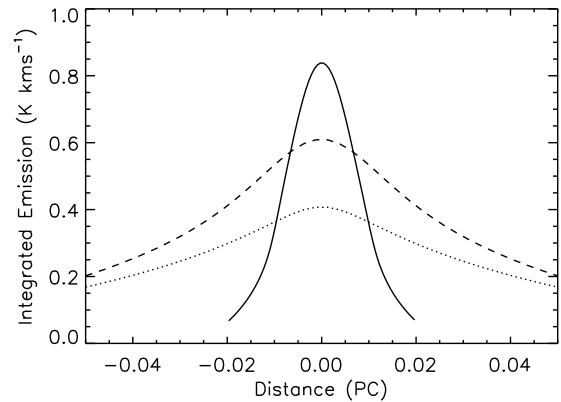
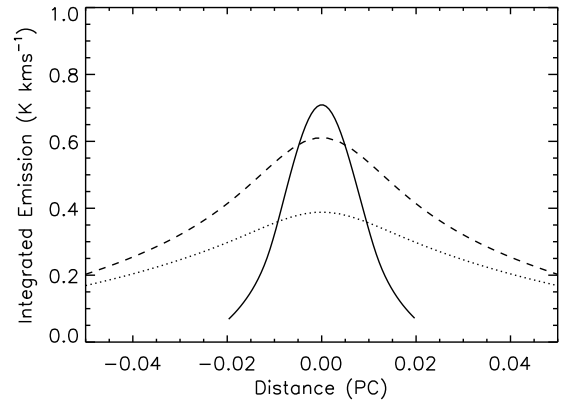
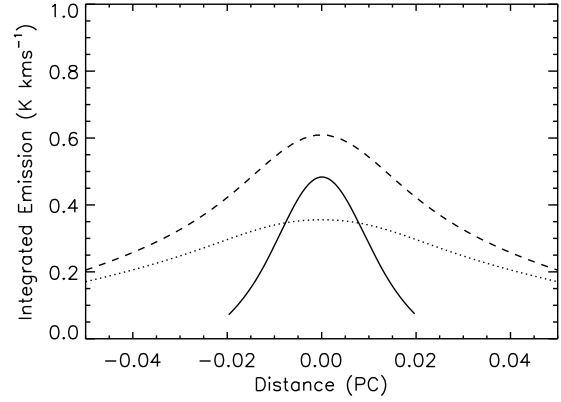


Figure 6. Trace of the integrated intensity of $\text{C}^{18}\text{O}(1-0)$ (dotted line), $\text{C}^{17}\text{O}(1-0)$ (dashed line), and $\text{N}_2\text{H}^+(1-0)$ (solid line), across our model of a subsonically contracting core. This figure shows the integrated intensities at 3 times in the evolution of the contraction, when the central density is $2 \times 10^6 \text{ cm}^{-3}$ (top), $2 \times 10^7 \text{ cm}^{-3}$ (middle), and $2 \times 10^8 \text{ cm}^{-3}$ (bottom). The internal structure of this model is shown in figure 3. The N_2H^+ emission has been divided by 5.65 and the C^{18}O emission by 3.65, the same as in figure 5.

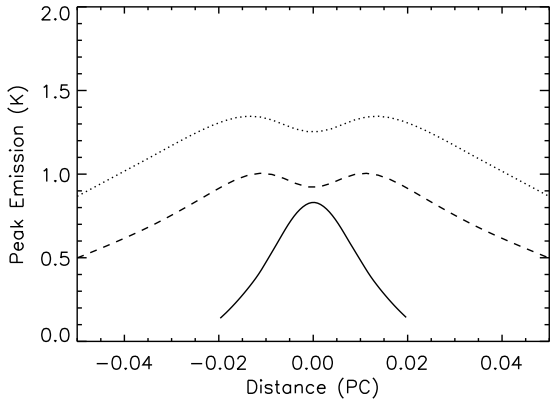
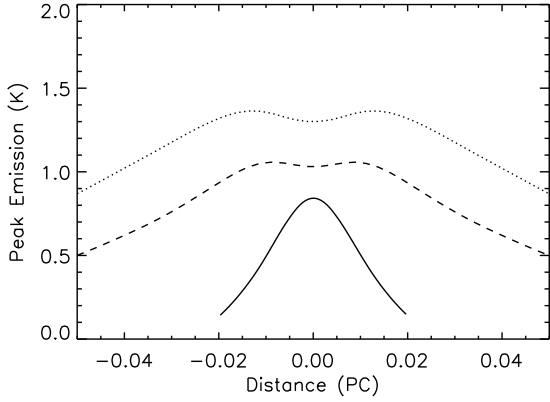
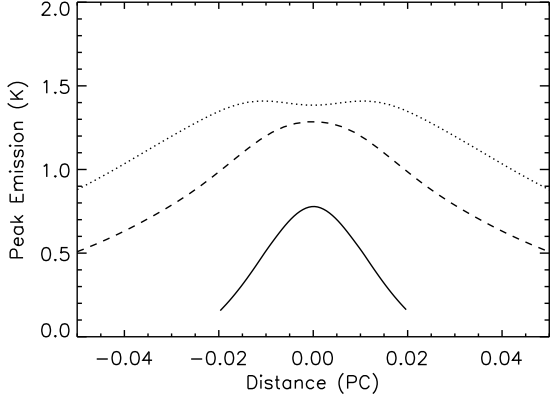


Figure 7. Trace of the peak brightness of $\text{C}^{18}\text{O}(1-0)$ (dotted line), $\text{C}^{17}\text{O}(1-0)$ (dashed line), and $\text{N}_2\text{H}^+(1-0)$ (solid line), across our model of a subsonically contracting core. This figure shows the peak brightness at 3 times in the evolution of the contraction, when the central density is $2 \times 10^6 \text{ cm}^{-3}$ (top), $2 \times 10^7 \text{ cm}^{-3}$ (middle), and $2 \times 10^8 \text{ cm}^{-3}$ (bottom). The internal structure of this model is shown in figure 3. The N_2H^+ emission has been divided by 5.65 and the C^{18}O emission by 3.65, the same as in figure 5. The ratio of the peak intensity of $\text{C}^{18}\text{O}(1-0)$ and $\text{C}^{17}\text{O}(1-0)$ is different than the ratios of the integrated intensities because the $\text{C}^{17}\text{O}(1-0)$ line is split into 3 hyperfine lines (figures 9).

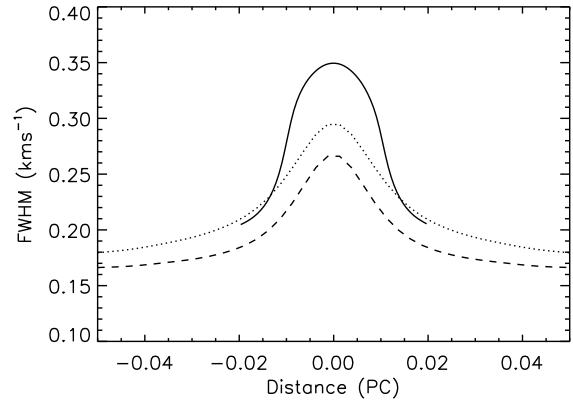
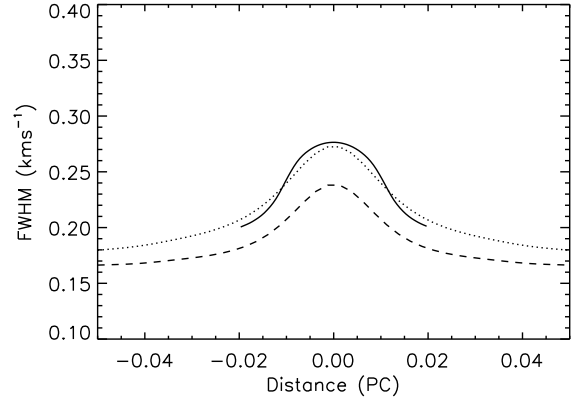
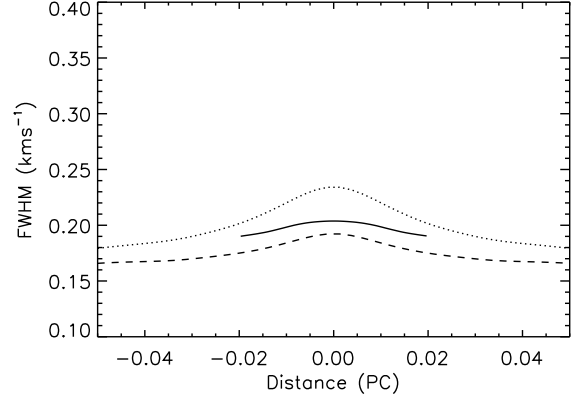


Figure 8. Trace of the FWHM of $\text{C}^{18}\text{O}(1-0)$ (dotted line), $\text{C}^{17}\text{O}(1-0)$ (dashed line), and $\text{N}_2\text{H}^+(1-0)$ (solid line), across our model of a subsonically contracting core. This figure shows the line width at 3 times in the evolution of the contraction, when the central density is $2 \times 10^6 \text{ cm}^{-3}$ (top), $2 \times 10^7 \text{ cm}^{-3}$ (middle), and $2 \times 10^8 \text{ cm}^{-3}$ (bottom). The figure shows that in the center of the core the predicted C^{18}O , C^{17}O , and N_2H^+ line widths increase by 0.074, 0.060, and 0.145 kms $^{-1}$, respectively because the infall velocities, unresolved by the observations increase as the core evolves. The internal structure of this model is shown in figure 3.

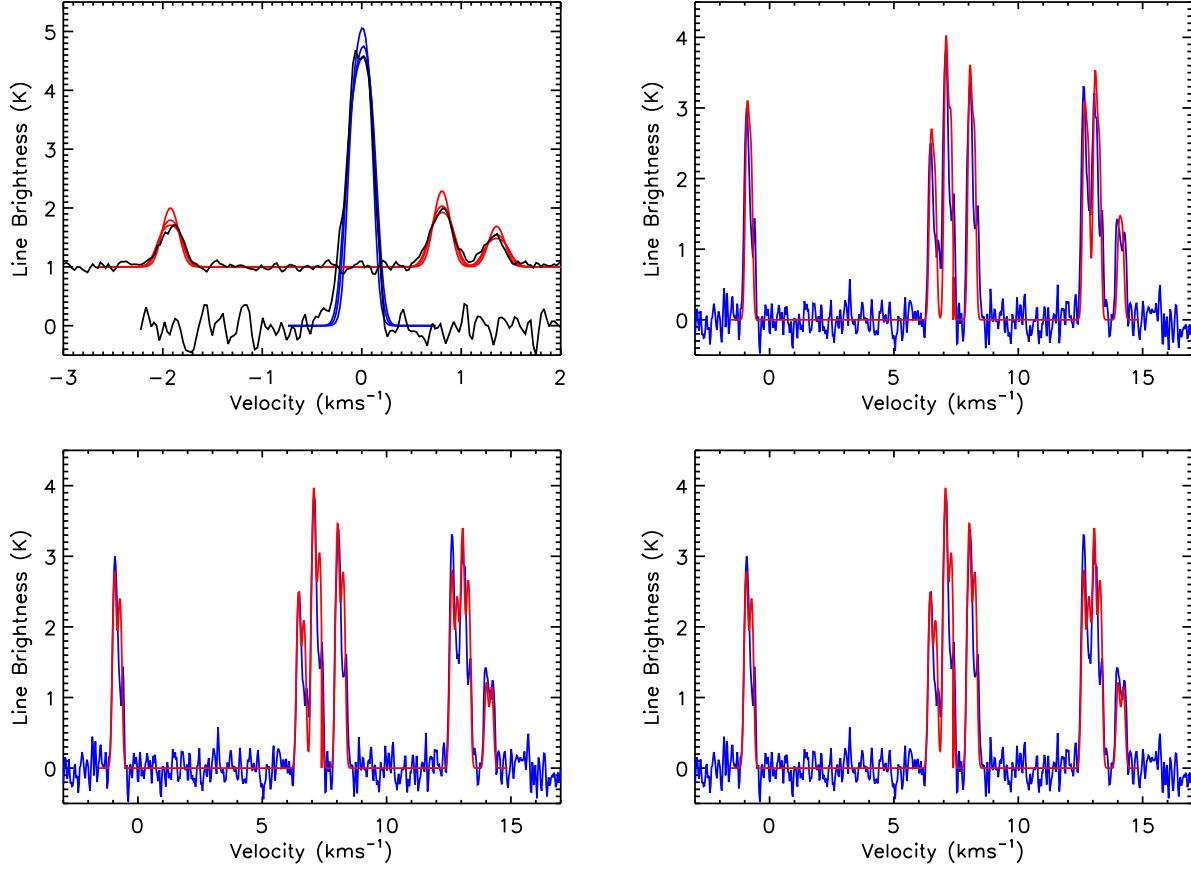


Figure 9. Spectra of CO(1-0) and $\text{N}_2\text{H}^+(1-0)$ at the center of our model of a subsonically contracting core. This figure shows the line emission at 3 times in the evolution of the contraction, when the central density is $2 \times 10^6 \text{ cm}^{-3}$, $2 \times 10^7 \text{ cm}^{-3}$, $2 \times 10^8 \text{ cm}^{-3}$. The *upper left* figure shows spectra of $\text{C}^{18}\text{O}(1-0)$ (*red*), $\text{C}^{17}\text{O}(1-0)$ (*blue*) at the 3 evolutionary times corresponding to the different densities. Also shown are the observed spectra (Caselli et al. 1999). The C^{17}O spectra have been shifted upward by 1 K. There is very little difference in the model CO spectra as the core evolves. The other 3 figures show the spectra of $\text{N}_2\text{H}^+(1-0)$ at the 3 times with one figure for each time: $2 \times 10^6 \text{ cm}^{-3}$ (*upper right*), $2 \times 10^7 \text{ cm}^{-3}$ (*lower left*), and $2 \times 10^8 \text{ cm}^{-3}$ (*lower right*). In these 3 figures, each N_2H^+ model spectrum (*red*) is shown together with the observed spectrum (*blue*). There is very little difference between the model spectra at the last two evolutionary times because the density increase is confined to a small region in the very center of the core. The internal structure of these models are shown in figure 3.